




# Effect of electric bias on trapping and release of excitons in GaN/(Al,Ga)N quantum wells

R. Aristegui , F. Chiaruttini, B. Jouault , P. Lefebvre , C. Brimont, T. Guillet , and M. Vladimirova   
*Laboratoire Charles Coulomb (L2C), University of Montpellier, CNRS, 34095 Montpellier, France*

S. Chenot, Y. Cordier , and B. Damilano   
*CRHEA, Université Côte d'Azur, CNRS, 06560 Valbonne, France*

 (Received 31 March 2022; revised 31 May 2022; accepted 16 June 2022; published 28 July 2022)

A giant built-in electric field in the growth direction makes excitons in wide GaN/(Al, Ga)N quantum wells spatially indirect even in the absence of any external bias. Significant densities of indirect excitons can accumulate in electrostatic traps imprinted in the quantum well plane by a thin metal layer deposited on top of the heterostructure. By jointly measuring spatially resolved photoluminescence and photo-induced current, we demonstrate that exciton density in the trap can be controlled via an external electric bias, which is capable of altering the trap depth. Application of a negative bias deepens the trapping potential, but does not lead to any additional accumulation of excitons in the trap. This is due to exciton dissociation instigated by the lateral electric field at the electrode edges. The resulting carrier losses are detected as an increased photocurrent and reduced photoluminescence intensity. By contrast, application of a positive bias washes out the electrode-induced trapping potential. Thus, excitons get released from the trap and recover free propagation in the plane that we reveal by spatially resolved photoluminescence.

DOI: [10.1103/PhysRevB.106.035429](https://doi.org/10.1103/PhysRevB.106.035429)

## I. INTRODUCTION

Indirect excitons (IXs) are bound pairs of an electron and a hole confined in separated quantum layers, either semiconductor quantum wells (QWs) [1,2], or various transition metal dichalcogenides (TMD) monolayers [3–6]. Due to their permanent dipole moment, IXs can be controlled *in situ* by voltage [6–8], can travel over large distances [5,9–13], and can cool below the temperature of quantum degeneracy before recombination [14–24]. Due to these properties, IXs are considered as a promising platform for the development of excitonic devices [25,26]. Most prominent, experimentally demonstrated devices operating via electrical bias control are based on GaAs. These include traps, lattices, and excitonic transistors [7,27–31].

Excitons in GaN/(Al,Ga)N QWs grown along the (0001) crystal axis are naturally indirect, as their electron and hole constituents are spatially separated in growth direction due to a strong built-in electric field [32–36]. As a result, GaN-based QWs differ from other heterostructures hosting indirect excitons – such as GaAs-based double QWs and recently developed TMD heterobilayers – where an external electric bias is usually applied to push the IX transition energy below that of the direct exciton [1,6,37,38].

We have shown previously that in-plane confinement and cooling of GaN-hosted IXs can be achieved without any applied electric bias via an electrostatic potential created by metallic patterns, of various shapes, deposited on the sample surface [39]. In contrast with GaAs and TMD-based systems, here IXs accumulate in the bare surface regions, rather than in the metal-covered areas [see Fig. 1(b)]. This amends the collection of light emitted by trapped IXs, and could be poten-

tially advantageous for IX coherence, since spurious electrons that inevitably emerge in the presence of an electric bias are known to be detrimental for trapped IX coherence properties [40–42].

In this work we start to exploit these advantages. IXs that we study are created optically in the plane of GaN QW. The sample surface is patterned with electrodes similar to those realized in Ref. [39], but here we apply to them an external electric bias, and detect both spatially resolved emission and the corresponding photocurrent. This allows us to demonstrate that (i) IXs can be released from the trap upon application of a positive bias due to reduction of the trap depth; (ii) application of a negative bias does increase the depth of the trap but fails augmenting IX accumulation; (iii) the efficiency of the IX density control by the external bias is limited by the increasingly high in-plane component of the electric field, that leads to IX dissociation in the presence of a strong, negative bias.

## II. SAMPLES AND EXPERIMENTAL SETUP

The studied sample is grown by molecular beam epitaxy on a free-standing (0001)-oriented GaN substrate (AMMONO, threading dislocation density  $\approx 10^4$  cm<sup>-2</sup>), followed by a 1200-nm-thick GaN buffer. It contains a wide GaN QW ( $d = 8$  nm) sandwiched between two identical Al<sub>0.07</sub>Ga<sub>0.93</sub>N barriers ( $b = 100$  nm), see Fig. 1(b).

The built-in electric field in the growth direction that we estimate as  $F_z \approx 450$  kV/cm [43] makes excitons in this QW spatially indirect. The electrons are pushed by this field towards the sample surface, while the holes move towards the substrate; this is the quantum-confined Stark effect [32]. As

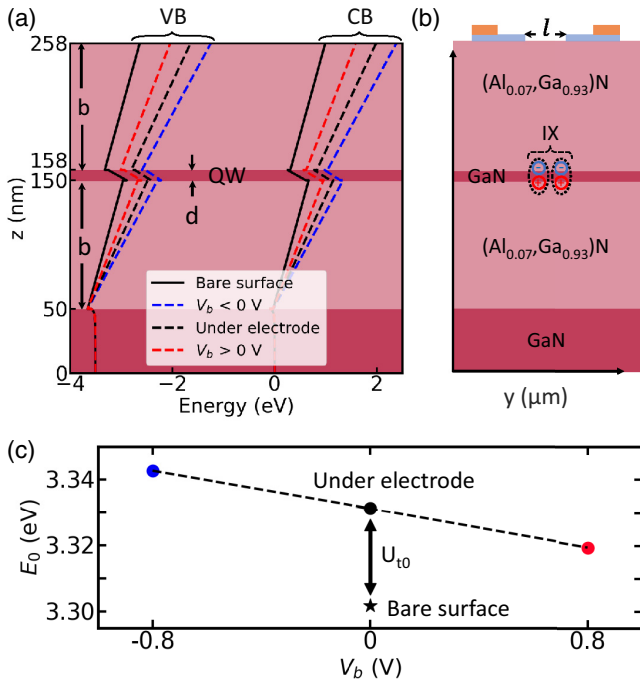


FIG. 1. (a) Calculated valence (VB) and conduction band (CB) diagrams for the studied sample in the absence (solid line) and in the presence (dashed lines) of the electrodes on the surface. (b)  $yz$  view of the sample covered by semi-transparent (5 nm Au/5 nm Ni, blue) and opaque (200 nm Au, orange) electrodes. (c) Calculated zero-density exciton energy in the electrode-covered regions at different voltages (circles) and in the bare surface areas (star). Arrow shows  $U_{t0}$ , the zero-density trapping potential depth, at  $V_b = 0$  V.

a consequence, in the zero-density limit, IX energy is as low as  $E_0 \approx 3.3$  eV, that is about 0.18 eV below GaN bandgap at 10 K. The corresponding radiative lifetime is in the order of microseconds, binding energy  $E_b = 18.6$  meV, and dipole length is close to the QW width [36,39,44].

In order to create an in-plane trapping potential, semi-transparent electrodes consisting of 5 nm of Au on top of 5 nm of Ni are evaporated on the sample patterned by photolithography. The shape of the electrodes is sketched in Fig. 2. The lateral dimensions are  $l = 10 \mu\text{m}$  and  $L = 145 \mu\text{m}$ . The electrodes ensure  $\approx 1$  eV Schottky barrier shift with respect to bare surface [39,45–47] and are used in state-of-the-art GaN/(Al,Ga)N high electron mobility transistors [48]. The energy band alignment, calculated using NextNano++ software [43], is affected by the electrodes as shown in Fig. 1(a). The black dashed line is calculated in the presence of the electrodes, while the solid line is calculated in their absence. The corresponding IX transition energies are shown in Fig. 1(c). The black star indicates the energy in the bare surface region and a black circle in the region covered by the electrodes. The energy gap between these two energies,  $U_{t0}$ , defines the depth of the trap in the absence of external bias and in the zero-density limit. The resulting zero-density in-plane potential at  $V_b = 0$  is shown in Fig. 3(b) by the black dashed line. The low-energy area, sandwiched between electrode-induced bumps of the potential, constitutes an electrostatic trap for IXs. The

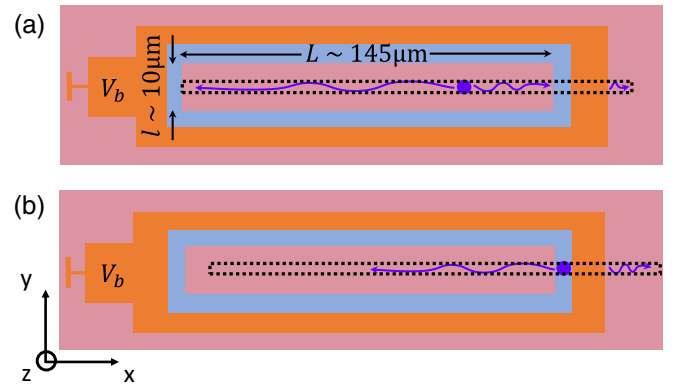


FIG. 2.  $xy$  view of the sample surface covered by electrodes and two experimental geometries: excitation on the bare surface within the trap (a) and through the semi-transparent electrode (b). Semi-transparent (opaque) electrodes are shown in blue (orange), their proportions are not strictly respected. Dashed frames indicate the detection area, circles indicate excitation positions, and arrows are propagating excitons which are optically detected

same technology has been used in Ref. [39] where electrostatic traps for GaN-hosted IXs have been demonstrated.

For application of an external electric bias, the outer part of the electrode surface is additionally covered by an opaque 200-nm-thick gold layer to which the wires are bonded. An electric bias  $V_b$  between  $-3$  V and 1 V is applied to the electrodes, while the naturally  $n$ -doped substrate ensures the common ground. The resulting current is measured in both the absence and presence of optical excitation. Positive electric

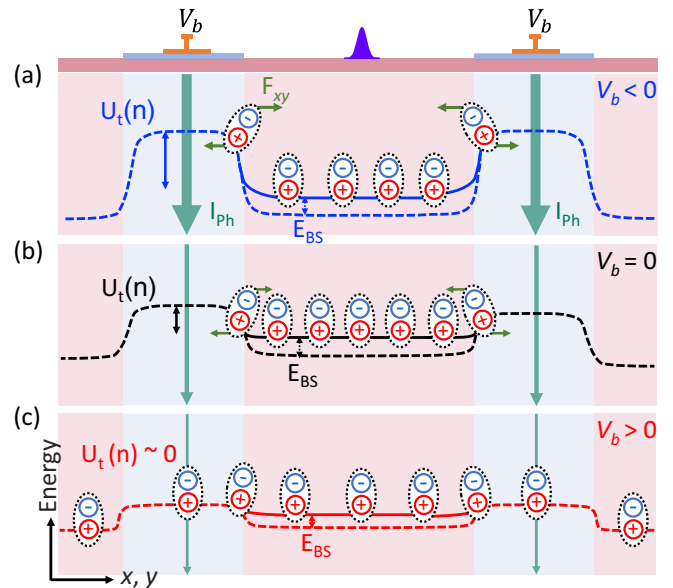


FIG. 3. Sketch of the IX energy profile along  $x(y)$  axis at negative (a), zero (b) and positive (c) applied biases  $V_b$  in the zero-density regime (dashed lines). The modifications of the energy profile induced by optical pumping are shown by solid lines. IX population, trap depth  $U_t(n) = U_{t0} - E_{BS}$ , IX blueshift  $E_{BS}$ , lateral component of the electric field  $F_{xy}$  at the trap edges and photocurrent  $I_{ph}$  are schematically represented.

bias reduces the Schottky barrier, while a negative bias has the opposite effect. Consequently, the energy bands shift as illustrated in Fig. 1(a). The red dashed line is calculated at positive bias, and the blue at a negative one. The corresponding IX energies are shown in Fig. 1(c) with the same color code. The resulting profiles of the in-plane potential at negative, zero, and positive biases are shown in Figs. 3(a)–3(c) by dashed lines. One can see that the application of a negative bias further enhances the potential barriers under the electrodes, while a positive bias smears them out. This effect provides the basis for IX density control by an external bias.

Importantly, due to their mutual repulsion, IXs created in the trap screen-out the trap potential  $U_{t0}$  [35,36,49]. This screening results in a blueshift  $E_{BS}$  of the IX energy in the trap:

$$E_{IX}(n) = E_0 + E_{BS}(n), \quad (1)$$

and in the reduction of the trap depth:

$$U_t(n) = U_{t0} - E_{BS}(n), \quad (2)$$

as shown in Fig. 3 by solid lines. When excitonic correlation effects are negligible,  $E_{BS}$  is usually assumed to be proportional to the IX density:

$$E_{BS}(n) = \phi_0 n. \quad (3)$$

For our sample  $\phi_0 = 11.2 \times 10^{-11}$  meV/cm<sup>-2</sup>. This value is extracted from the self-consistent solution of the Schrödinger and Poisson equations, see the Appendix [43]. Equations (1) and (3) allow us to monitor the variations of the IX density.

Another important effect that needs to be accounted for is the exponential dependence of the electron and hole wave functions overlap on the IX density. It leads to an exponential relation between IX emission intensity  $I$  and its energy blueshift  $E_{BS}$  [17,36,39,50,51]:

$$I \propto E_{BS} \exp(E_{BS}/\gamma\phi_0). \quad (4)$$

We estimate  $\gamma = 1.9 \times 10^{11}$  cm<sup>-2</sup> for our sample (see the Appendix).

The sample is placed in a cold-finger cryostat and cooled to 10 K. Optical excitation is provided by a continuous wave laser focused in a  $\approx 1$   $\mu$ m-diameter spot on the sample surface, which we locate either within the trap on the bare surface, or on the semitransparent electrode, see Figs. 2(a) and 2(b), respectively. The excitation wavelength,  $\lambda = 355$  nm, is situated very close to the GaN bandgap energy, but well below the emission energy of the Al<sub>0.07</sub>Ga<sub>0.93</sub>N barriers, to avoid spurious charge carriers in the structure. The microscope objective collects the photoluminescence (PL) signal. The image of the sample surface is reproduced at the entrance of a spectrometer, where it is filtered by a vertical entrance slit. This setup provides a direct spatial imaging of the PL with  $\approx 0.8$   $\mu$ m spatial and  $\approx 1$  meV spectral resolution.

### III. EXPERIMENTAL RESULTS AND DISCUSSION

The presentation of experimental results is structured in two parts. In Sec. III A we analyze how an applied electric bias modifies the in-plane potential pattern imposed by the electrodes. In the second part we determine to which extent

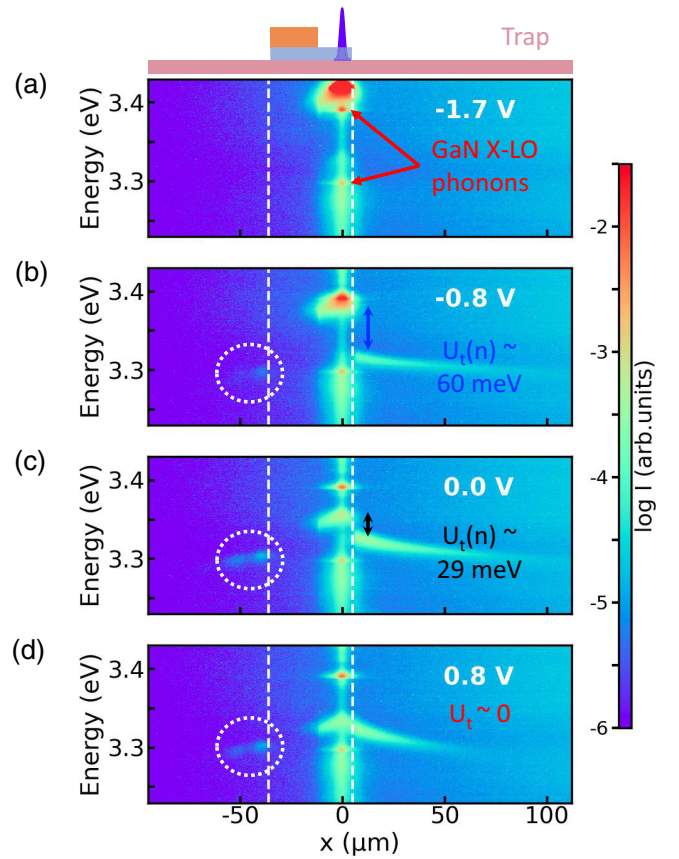


FIG. 4. Spatially resolved PL spectra (color encoded in log scale) measured upon excitation through the semi-transparent electrode at different values of the applied electric bias  $V_b$ . Both laser spot and electrode positions are indicated on top with the same color code as in Fig. 1(b). Vertical dashed lines delimit electrode-covered area. Dashed circles highlight emission of IXs coming from outside of both the trap and the electrode-covered area.

the IX density in the trap can be controlled by an applied electric bias (Sec. III B).

#### A. General operation of the electrostatic trap

In order to explore how the in-plane potential experienced by IXs is affected by the applied bias, we start from the measurements in the configuration shown in Fig. 2(b); the excitation spot is located on top of the semitransparent electrode. This choice of the excitation geometry allows us to monitor the bias-induced potential variations via the energy of the IX emission passing through the semitransparent electrode.

Figure 4 shows color encoded (logarithmic scale) PL spectra measured at various distances from the laser spot along the  $x$  axis. Measurements at four different values of the electric bias are shown, the incident power is  $P = 3.8$  mW. The entire set of data comprising all the values of the applied bias is available as Supplemental Material [52].

Let us first consider the measurements at  $V_b = 0$  V. Under the excitation spot the emission is extremely broad. On top of this broad emission two very narrow peaks can be distinguished, at 3.390 eV and at 3.298 eV. They show up in all the spectra measured in this work, and can be attributed to one and

two LO phonon replicas of the free exciton state in bulk GaN, respectively. The broader peak at  $\approx 3.355$  eV corresponds to IXs emitting directly under the excitation spot through the semi-transparent electrode.

Excitonic emission can be observed on both sides of the excitation spot. Its energy decreases continuously because the density of IXs decreases when they spread away from the excitation spot due to mutual repulsion. To the left from the spot, in the area covered not only by the thin, but also by the thick gold electrode, no optical emission is detected. Further away, in the bare surface region at the border of the gold electrode, weak bias-independent IX emission at  $\approx 3.3$  eV can be distinguished. It is pointed out by the white dashed circle.

To the right from the excitation spot, at  $\approx 5 - 6$   $\mu\text{m}$ , diffusing IXs reach the electrode edge and fall into the trap. Their emission energy suddenly drops by  $\approx 29$  meV. This drop corresponds to  $U_t(n)$ , the in-plane potential barrier created by the electrodes and partly screened out by the trapped IXs, see Eq. (2) and Fig. 3(b). Further away the IX emission energy decreases continuously due to a reduction of the IX density via optical recombination and diffusion in the trap.

Application of the positive bias  $V_b = 0.8$  V dramatically affects the emission pattern, see Fig. 4(d). Indeed, the emission energy under the excitation spot decreases, and the steep drop of the IX energy at the electrode border smears out. By contrast, application of the same, but negative bias  $V_b = -0.8$  V [Fig. 4(b)] produces the opposite effect. The emission energy under the excitation spot increases and the energy drops stronger at the electrode edge,  $U_t \approx 60$  meV. This is consistent with the idea presented schematically in Fig. 3: a positive bias reduces the trap depth and thus the energy difference between IXs emitting under the electrodes and in the trap, while the negative bias affects the in-plane potential in the opposite way.

Under negative bias higher than a critical value  $V_{bc} = -1.6$  V, the PL of IXs is almost entirely quenched, see Fig. 4(a). We attribute this quenching to the in-plane component of the electric field that builds up at the electrodes edges and gives rise to IX dissociation [28]. This mechanism of nonradiative losses is discussed in more detail in Secs. III B and A 3.

The photocurrent and the IX emission energy measured under the excitation spot are shown in Fig. 5 as a function of the applied bias. One can see that when changing the bias from positive to negative, the photo-current  $I_{ph}$  increases up to almost 1  $\mu\text{A}$  at  $V_{bc} = -1.6$  V, where it saturates. The increase of  $I_{ph}$  is accompanied by the increase of the IX emission energy under the excitation spot, that is in the electrode-covered region. The blue dashed line in Fig. 5 shows the linear fit of the IX energy dependence on the applied bias. The resulting slope,  $\mathcal{R}_e = 38$  meV/V, can be compared with the simple estimation assuming that all the applied voltage drops linearly between the surface and GaN buffer situated  $\mathcal{L} = d + 2b = 208$  nm below. This yields  $\mathcal{R}_e = ed/\mathcal{L} = 38$  meV/V, where  $e$  is the absolute value of the electron charge. This is in perfect agreement with the experimentally measured rate [53].

By contrast, at strong negative bias, above  $V_{bc} = -1.6$  V, where IX transport and emission from the trap are quenched, the energy variation rate decreases abruptly down to  $\mathcal{R}_e = 6.7$  meV/V. The corresponding photo-current saturates (red symbols), while the dark current (not shown) continues to grow

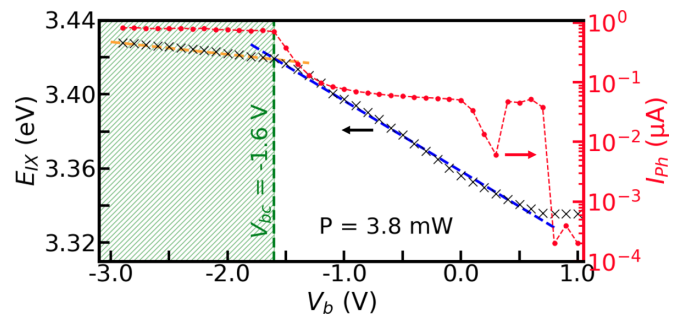


FIG. 5. Left-hand axis: bias dependence of the IX emission energy measured under the excitation spot ( $x = 0$ ) in the same geometry as in Fig. 4 (crosses). Dashed lines are linear fits of  $E_{IX}$  above (blue) and below (orange) the critical voltage  $V_{bc}$ . Right-hand axis: bias dependence of the corresponding photo-induced current (red circles). The hatched area shows the range of applied biases where photocurrent saturates.

linearly with increasing bias. This suggests that the majority of the photo-carriers is extracted from the system in the  $z$  direction via the photocurrent. These nonradiative losses also limit IX accumulation when they are directly created in the trap, as will be discussed in Sec. III B.

Thus, we have an experimental demonstration that, at least at  $V_b > V_{bc}$ , an external bias effectively modifies the potential experienced by IXs under the electrodes. Nevertheless, the following legitimate question arises. Does the bias have any effect on the potential in the bare surface regions, that is within the trap? One can see in Fig. 4 that IX density varies substantially across the trap at a given bias and is also bias dependent. Therefore, it is not trivial to disentangle the bias and the density effects on the resulting potential profile, and a neat solution should be found.

To do so we take advantage of the fact that under a given surface potential (or, equivalently, fixed value of the built-in electric field along the growth axis) the relation between IX emission energy  $E_{IX}$  and its intensity  $I$  is expected to obey Eqs. (1) and (4) for any IX density. In order to extend the range of accessible IX energies and intensities we analyze the experiments where laser excitation is situated inside the trap, see Fig. 2(a). The corresponding spatially resolved PL emission maps at four different values of  $V_b$  are shown in Figs. 6 and 7. Note that to avoid undesirable effects of the laser-induced heating of excitons we limit our consideration to the spatial area situated at more than 10  $\mu\text{m}$  away from the excitation spot.

Figure 8 shows integrated IX emission intensities measured at different positions within the trap as a function of the corresponding emission energies. Both energies and intensities are determined by fitting the phenomenological function, introduced in Ref. [44] and also reported in the Appendix, to the IX emission spectra. The data obtained at three different values of  $V_b$  are presented.

The analysis of the dependences shown in Fig. 8 in terms of Eqs. (1), (3), and (4) allows us to quantify to which extent the electrostatic potential in the bare surface regions is affected by the applied bias, and to reveal potential variations of  $E_0$  and  $E_r \equiv \phi_0\gamma$  which are not expected from our simple modeling

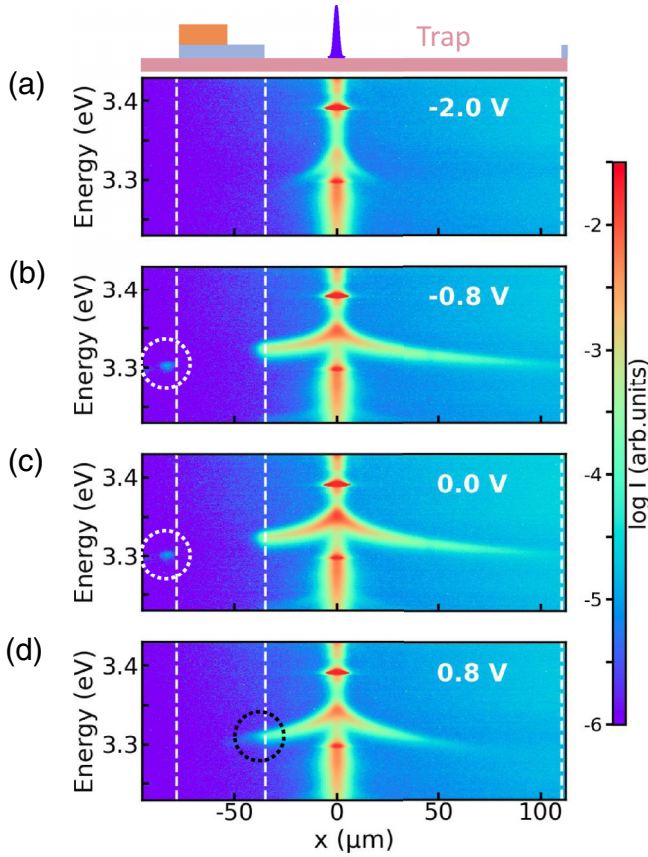


FIG. 6. Spatially resolved PL spectra (color encoded in log scale) measured upon excitation at  $x = 0$  at different values of the applied electric bias  $V_b$ . Excitation power is  $P = 2.4$  mW. Excitation spot and electrode positions are indicated on the top with the same color code as in Fig. 1(b). Vertical dashed lines delimit electrode-covered area. Dashed circles point IX emission from outside of the trap (white) and from the area covered by the electrodes (black).

[54]. The results of the fitting procedure are shown by lines in Fig. 8. The summary of  $E_0$  and  $E_r$  values in the entire range of accessible bias voltages is given in the inset.

One can see that  $E_r \approx 100$  meV remains constant within the error bars, while  $E_0$ , apart from the point at  $V_b = -1.8$  V, seems to decrease slightly when the bias is changed from zero to positive values [55]. However, the variation of  $E_0$  remains much weaker than that of the trapping potential  $U_{t0}$ , suggesting that it could be neglected.

It is instructive to notice that at lowest emission energies – mainly measured at largest distances from the excitation spot or at low excitation power – the dependence of the IX emission intensity on its energy  $I(E_{IX})$  starts deviating from the exponential behavior typical for two-dimensional systems, cf. Eq. (4). This points to the onset of the IX localization on the in-plane disorder potential at low IX densities. Indeed, due to strong built-in electric field in the growth direction, the amplitude of the localizing potential resulting from both (Al,Ga)N alloy composition and QW width fluctuations can reach 10 – 20 meV even in the best quality samples [56].

In Appendix A2 we analyze the relation between the IX emission energy and its linewidth (defined here as full width at

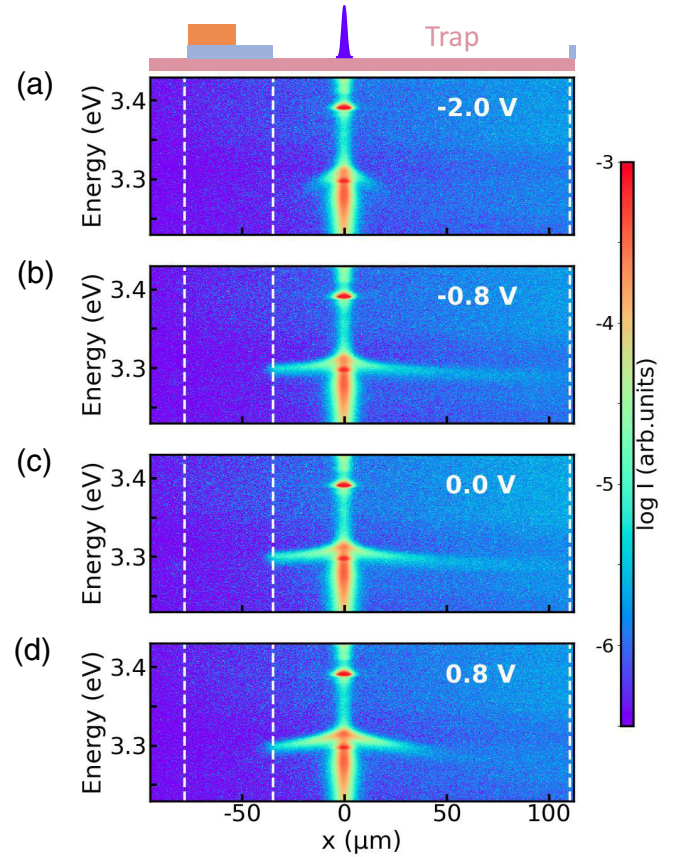


FIG. 7. Spatially resolved PL spectra (color encoded in log scale) measured upon excitation at  $x = 0$  at different values of the applied electric bias  $V_b$ . Excitation power is  $P = 0.6$  mW. Excitation spot and electrode positions are indicated on the top with the same color code as in Fig. 1(b).

half maximum (FWHM) of the exciton emission line) and unravel homogeneous and inhomogeneous contributions to the IX linewidth. This analysis corroborates the idea that fundamental properties of IXs inside the trap remain unaffected by the external bias. Thus, weak variations of  $E_0$  and  $E_r$  will not be accounted for in the estimations of the trapped IX densities reported below. We conclude that  $E_0 = 3.300 \pm 0.006$  eV for any  $V_b$ , while the trapping potential varies in the presence of the external bias at the rate  $R_e \approx 38$  meV/V.

## B. Bias-controlled exciton trapping and release

Let us now address the efficiency of the IX density control by the external bias and identify the conditions that maximize and minimize the density of IXs accumulating in the trap.

For this purpose we analyze the emission of IXs created directly within the trap at two different powers,  $P = 2.4$  mW and  $P = 0.6$  mW. The corresponding PL maps are shown in Figs 6 and 7, respectively. The same set of data was used in the the analysis reported in Fig. 8. The entire set of the data corresponding to all the values of the applied bias is available as Supplemental Material [57].

The main features that we observe are the following: (i) at zero applied bias, as well as at  $V_b = -0.8$  V, IXs accumulate at the left-hand trap edge. This is evidenced by the

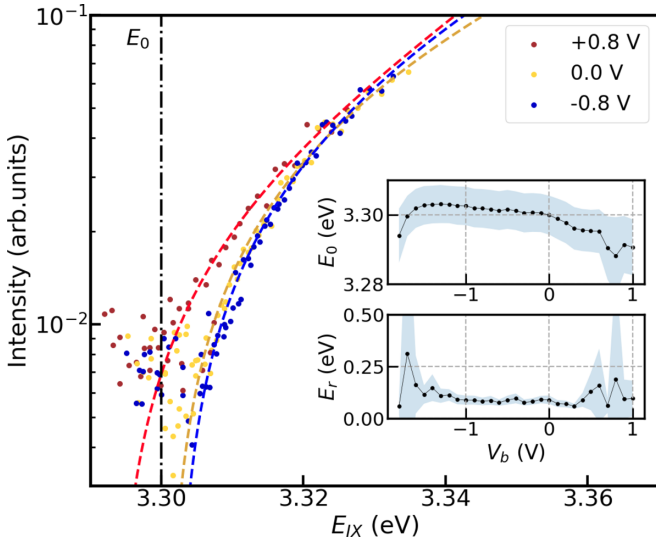


FIG. 8. Spectrally integrated intensity of the IX emission as a function of its peak energy, extracted from the experiments as those shown in Figs. 6 and 7 (excitation within the trap) at  $V_b = 0$  and at  $V_b = \pm 0.8$  V. Different energies correspond to different positions in the plane of the QW and we restrict our consideration to the points at  $x > 0$  separated from the excitation spot by more than  $10 \mu\text{m}$ . Dashed lines are fit to the data for each value of  $V_b$  using Eqs. (1) and (4). Inset shows  $E_0$  and  $E_r = \gamma\phi_0$ , obtained from the fitting procedure at different values of the applied bias.

spatial asymmetry of the emission energy (or, equivalently, IX density) profile. At higher excitation power a fraction of these accumulated IXs escapes from the trap and emits light outside the electrode-covered area. Their energy is close to the zero-density exciton energy  $E_0 = 3.3$  eV. This emission is pointed out by white dashed circles. (ii) At high negative bias  $V_b = -2$  V the emission is strongly quenched, in the same way as in the case of excitation through the electrode, cf. Fig. 4(a). (iii) At positive bias  $V_b = 0.8$  V the IX density distribution around the excitation spot is much more symmetric than at zero bias. This is consistent with the reduction of the trap depth at positive bias that is also observed in Fig. 4(d).

To quantify the efficiency of the IX trapping we show in Fig. 9 the total number of IXs within the detection area in the trap as a function of the applied bias. The detection area  $-(2 \times 145) \mu\text{m}^2$ , that is  $\approx 20\%$  of the total trap area—is shown schematically in Fig. 2(a) by the black dashed line. For both excitation powers IX populations are given in percent of  $N_0$ , the number of IXs measured at  $V_b = 0$  and  $P = 2.4$  mW. Using Eq. (1) with  $E_0 = 3.3$  eV it can be estimated as  $N_0 \approx 2.6 \times 10^{13}$  particles. Note that only IXs emitting at energies above  $E_0$ , which are supposed to be delocalized, are taken into account (see Sec. III A and Appendix A 2).

One can see in Fig. 9 that the population of IXs in the trap does not grow up at negative bias. Moreover, IX population decreases sharply above a critical bias  $V_{bc}$ , in concert with the saturation of the photocurrent. The latter is shown on the right-hand scale of Fig. 9. As mentioned in Sec. III A and sketched in Fig. 3, we explain this effect as being due to IX dissociation induced by the in-plane component of the electric field  $F_{xy}$  that builds up at the electrode edges. The

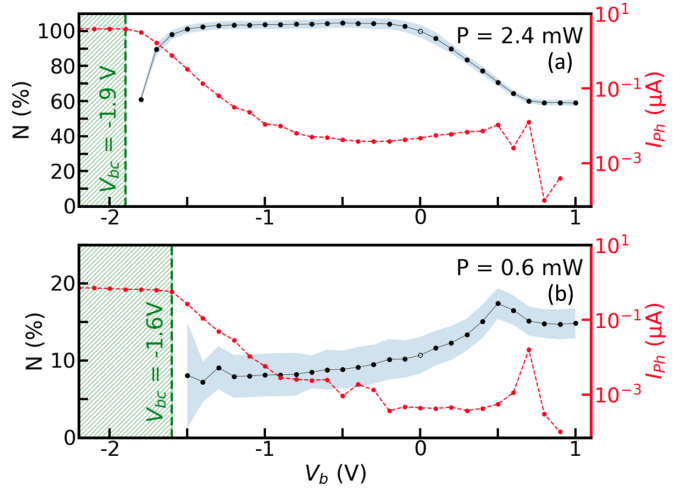


FIG. 9. Number of IXs within the detection area covering  $\approx 20\%$  of the trap (reported in percents of  $N_0$ , IX population measured at excitation power  $P = 2.4$  mW and  $V_b = 0$ , left scale) and the corresponding photo-current (right scale) as a function of the applied bias. IXs are created directly in the trap either at  $P = 2.4$  mW (a) or at  $P = 0.6$  mW (b). Hatched area shows the range of applied biases where photo-current saturates. Representative PL spectra corresponding to this analysis are shown in Figs. 6 and 7.

interpretation of this phenomenon within the drift-diffusion model coupled to bias-dependent nonradiative losses allows us to reproduce the experimental results at least qualitatively, see Appendix A 3.

Importantly, the critical bias is density dependent, it decreases with the excitation power:  $V_{bc} = -1.9$  V at  $P = 2.4$  mW and  $V_{bc} = -1.6$  V at  $P = 0.6$  mW. This can be understood as follows. At high power IXs accumulated in the trap partly screen out the trap potential  $U_{i0}$  imprinted by the electrodes, so that  $U_i(n) < U_{i0}$ . As a result, the trap depth is reduced by  $E_{BS}$ , see Eq. (2) and Fig. 3. Therefore, at a given bias the in-plane field  $F_{xy}$  leading to exciton dissociation and losses via photo-current is reduced as well. Thus, the critical value of  $F_{xy}$  such that the photocurrent dominates over the radiative recombination in the decay of the IX population is reached at a higher negative bias in the strongly excited trap.

Another effect of the pumping power on the trapping efficiency manifests itself at positive bias. Indeed, as one can see in Fig. 9(a), at high power IXs are efficiently released from the trap when a positive bias is applied, their population is reduced by  $\approx 40\%$ . In contrast, at low power [Fig. 9(b)] IX population remains constant. We argue that this is because, at low densities, close to the localization threshold, IX diffusion is not efficient enough to allow them to escape from the trap.

Altogether, while we could not alter IX population in the trap by applying a negative bias, application of a positive bias allowed us to unload IXs from the trap, here up to 40%. The implementation of such control appears to depend crucially on the trap filling because it relies on efficient diffusion, which is density-activated [36]. The optimum trapping conditions, characterized by maximum IX density collected within the trap, are reached at zero applied bias. This differs advantageously from GaAs and TMD-based systems hosting IXs, where application of the bias is a prerequisite for IX trapping.

#### IV. SUMMARY AND CONCLUSIONS

In conclusion, we have studied the effect of an external electric bias on the operation of the electrostatic trap for IXs. Such device is formed by metallic gates deposited on the surface of polar GaN/(AlGa)N QW. The particularity of this type of QWs consists in a strong built-in electric field, typically several hundreds of volts per centimeter. It has been demonstrated earlier that deposition of metallic gate reduces this field, so that in contrast with their GaAs-hosted counterparts, IXs in GaN/(AlGa)N QWs get trapped in the regions of the QW plane that are not covered by electrodes.

In this work we have shown that the trapping potential can be additionally controlled by the external electric bias. In a similar way as in GaAs-based devices developed for IX trapping, when a bias is applied between the  $n$ -doped substrate and the metallic gate, IX energy levels in the QW are pushed either up or down, depending on the sign of the applied bias. The resulting variation of the in-plane trapping potential of order of several tens of millielectronvolts has been evidenced by spatially-resolved  $\mu$ PL spectroscopy across semitransparent electrodes. These experiments also demonstrate that IX energy in the bare surface regions is only weakly affected by the bias.

The accumulation of IXs in the trap at negative voltages, where the trap gets deeper, appears to be inhibited by the nonradiative losses resulting from the in-plane component of the electric field in the vicinity of the electrode edges. These losses are detected as a photocurrent that grows exponentially with increasing negative bias. Above the IX density-dependent critical value of negative bias these non-radiative losses overcome radiative recombination. At this point the excitonic PL suddenly drops, and the photocurrent saturates. Thus, at least within the current device geometry it is not possible to increase the IX density in the trap by applying an external electric bias. The modifications in the device design that we anticipate to overcome this problem and reduce the in-plane field include the positioning of the QW closer to the homogeneous bottom  $n$ -type layer, as suggested in Ref. [28].

Application of positive voltages, that reduce both the trap depth and spurious in-plane electric field, allows us to release IXs out of the trap. Here the limitation is only imposed by the IX density, that needs to be sufficiently high. Indeed, at low IX densities the disorder-driven localization hinders IX diffusion. Consequently, IXs cannot move away from the trap during their lifetime and their population inside the trap does not change despite the reduced trap depth. Working with smaller traps could extend the density range where IXs release from the trap remains effective.

Finally, since IX diffusion in GaN/(AlGa)N QWs over tens of micrometers can be monitored optically, future work in the optimized devices may include room temperature IX density control by the external bias. This paves the way towards IX-based optoelectronic devices. On the other hand, provided that nonradiative losses related to electrode edges could be reduced, more complex multielectrode devices, inspired by GaAs-based technology, but taking advantage of GaN particularities, may be interesting to address in the future.

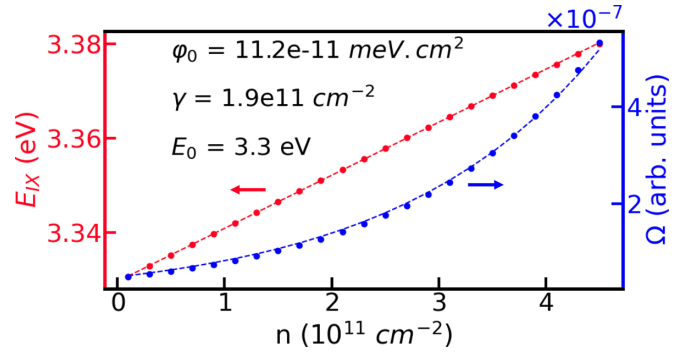


FIG. 10. Electron-hole pair energy (red) and squared overlap integral (blue) calculated using NextNano++ software as a function of the carrier density.

#### ACKNOWLEDGMENTS

This work was supported by French National Research Agency via IXTASE (ANR-20-CE30-0032) and LABEX GANEXT projects, as well as by Occtanie Region through the Quantum Technology Challenge grant.

#### APPENDIX

##### 1. Density dependence of IX energy and radiative recombination rate

Figure 10 shows density dependence of the electron-hole pair energy (red symbols) and of the squared overlap integral (blue symbols) calculated for the sample under study using NextNano++ software [43]. The pair energy varies linearly with the density. The corresponding slope is estimated as  $\phi_0 = 11.2 \text{ meV}/10^{11} \text{ cm}^{-2}$ , see red dashed line. We assume that at not-too-high densities addressed in this work the IX binding energy is almost density independent so that the variation of IX energy with density is also linear and given by the same parameter:  $E_{IX} = E_0 + E_{BS} = E_0 + \phi_0 n$ .

The calculated density dependence of the squared overlap integral  $\Omega(n)$ , and thus of the radiative lifetime of the electron-hole pair  $\tau_R(n)$ , exhibits exponential behavior:  $\Omega(n) \propto 1/\tau_R \propto \exp(n/\gamma)$ , see the blue dashed line [35,49]. Fitting procedure yields  $\gamma = 1.9 \times 10^{11} \text{ cm}^{-2}$ . Since the integrated IX emission intensity is given by  $I = n/\tau_R(n)$ , the relation between the intensity and the energy takes the form given by Eq. (4). Note that in addition to one-dimensional calculations reproducing infinite-plane heterostructure in the  $z$  direction, NextNano++ offers the opportunity to calculate the electronic structure of the entire sample, including the whole heterostructure along the growth direction, and the top electrodes defining the electrostatic trap. Such calculations are needed to estimate the in-plane component of the electric field  $F_{xy}$  acting on the electron and hole constituents of the IX in the vicinity of the electrode edges. This field governs the nonradiative recombination of IXs that needs to be accounted for in the model presented in Appendix A 3.

##### 2. Density dependence of the IX linewidth

The determination of exciton densities has always been a thorny issue. In this work we tentatively rely on a combination

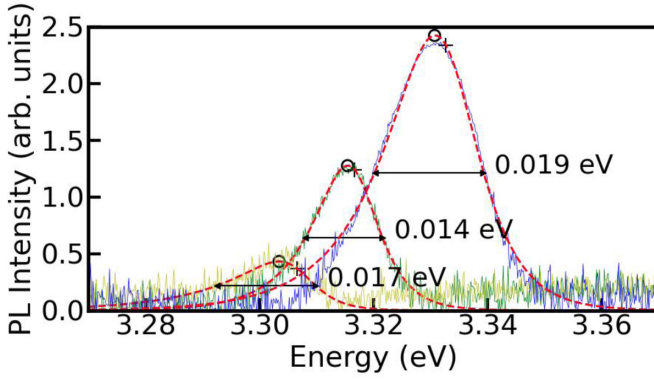


FIG. 11. PL spectra measured at zero bias at three different distances from the excitation spot (blue: 15  $\mu\text{m}$ , green: 45  $\mu\text{m}$ , yellow: 95  $\mu\text{m}$ ), extracted from Fig. 6(c). Red dashed lines show the fits to Eq. (A4). For each spectrum, values of  $E'_{IX}$  (crosses) and the PL peak maximum  $E_{IX}$  (circles) are indicated.

of two facts. (i) The IX emission energy shift  $E_{BS} = E_{IX} - E_0$  increases linearly with the density, at least in the absence of the excitonic correlation effects [21,31,58–61]. (ii) The relation between the IX density and intensity can be used to determine the zero-density energy  $E_0$ , so that  $n = E_{BS}/\phi_0$ . In the materials with high localization energies, the zero-density energy  $E_0$  ought to be interpreted as the lowest energy below which excitons are essentially localized.

To further confirm and complement the determination of  $E_0$  from the analysis of the IX emission intensity reported in Sec. III A, we consider here the linewidth of the IX emission. The latter appears to be strongly density dependent. Typical PL spectra measured within the trap at three different distances from the excitation spot at  $V_b = 0$  are shown in Fig. 11. Remarkably, the dependence of the linewidth on the emission energy (and thus on the density) is nonmonotonous. We suggest that this is due to interplay between homogeneous,  $\Gamma_h$ , and inhomogeneous,  $\Gamma_i$ , components of the linewidth:

$$FWHM = \sqrt{\Gamma_h^2 + \Gamma_i^2}, \quad (\text{A1})$$

that evince opposite density dependencies [62]. Indeed, at low density the disorder-induced inhomogeneous broadening dominates the linewidth. The increasing density tends to screen out the disorder, leading to the reduction of the IX linewidth down to some density-independent value [62–64]. We model this effect by the phenomenological function:

$$\Gamma_i = \Gamma_{i0}(1 + \exp(-E_{BS}/\sigma_i)). \quad (\text{A2})$$

In contrast, as far as IXs are localized,  $E_{IX} < E_0$ , the homogeneous contribution to the linewidth  $\Gamma_{h0}$  is close to zero,  $\Gamma_{h0} < 0.1$  meV. It is expected to increase at  $E_{IX} > E_0$ , and eventually to take over the inhomogeneous contribution. This is due to collisional broadening, which increases linearly with IX density [40,65,66]:

$$\Gamma_h = \Gamma_{h0} + \sigma_h E_{BS}. \quad (\text{A3})$$

Here we define  $E_{BS} \equiv 0$  for  $E_{IX} < E_0$ .

The simple model described above allows us to analyze the linewidth dependence on the energy, and extract relevant

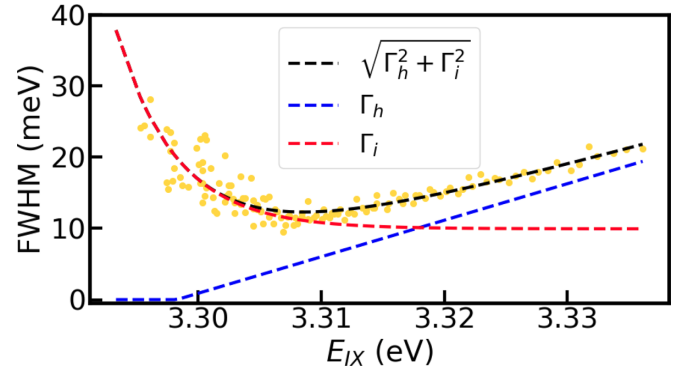


FIG. 12. Dependence of the IX linewidth (symbols) on its energy extracted from spatially resolved PL at zero applied bias shown in Fig. 6(c), and the corresponding fit to Eq. (A1) (black line). Blue and red lines show homogeneous and inhomogeneous contributions to the FWHM, respectively.

parameters, in particular  $E_0$  and its eventual bias dependence. We proceed as follows. First of all we determine the IX properties – emission energy  $E_{IX}$ , integrated intensity  $I_{IX}$  and FWHM – by fitting the function:

$$I_{PL}(E) \propto \frac{\exp(E'_{BS}/\beta_1)}{1 + \exp(E'_{BS}/\beta_2)} \quad (\text{A4})$$

to each spectrum. Here  $\beta_1$ ,  $\beta_2$ , and  $E'_{BS}$  are fitting parameters. Note, that the energy  $E'_{IX} = E_0 + E_{BS}$  does not coincide with the maximum of the PL intensity  $E_{IX}$ , see Fig. 11.

For each value of the applied bias, the dependence of the FWHM on  $E_{IX}$  can thus be analyzed. A representative example of such analysis at  $V_b = 0$  is shown in Fig. 12. Both homogeneous (blue) and inhomogeneous (red) contributions to the line broadening obtained from fitting of Eqs. (A1)–(A3) to the data are shown. This offers an alternative way to determine the zero-density IX energy, that we refer to as  $\tilde{E}_0$ . At  $V_b = 0$  we obtain  $\tilde{E}_0 = 3.298$  eV, very close  $E_0 = 3.300$  eV. According to this analysis, the inhomogeneous broadening dominates IX linewidth up to almost 20 meV above zero-density energy.

Figure 13 shows the dependence of IX linewidth on its energy for three values of  $V_b$ , as well as the corresponding fits to Eqs. (A1)–(A3). The inset summarizes the resulting values of  $\tilde{E}_0$  (red), and compare them to zero-density energy  $E_0$  (black) extracted from the integrated intensity data. It appears that the two methods used to determine zero-density energy yield quite similar results, corroborating its negligible dependence on the applied bias. Therefore, for tentative estimation of the IX densities shown in Figs. 9 and 14 we use a constant energy  $E_0 = 3.3$  eV for all the values of applied bias.

Finally, it is worth noting that the parameters of the homogeneous broadening  $\sigma_h \approx 0.5 \pm 0.1$  [see Eq. (A3)], as well as of the inhomogeneous broadening  $\Gamma_{i0} = 10 \pm 2$  meV and  $\sigma_i = 0.005 \pm 0.002$  [see Eq. (A2)], that we deduce from the fitting procedure do not show any bias dependence. This may indicate that collisional broadening of IXs in the trap is governed by either exciton-exciton or exciton-impurity, rather than exciton-electron collisions. One can compare  $\sigma_h$  with the simplest theoretical estimation  $\sigma_h = e\phi_0 D_s$ , where



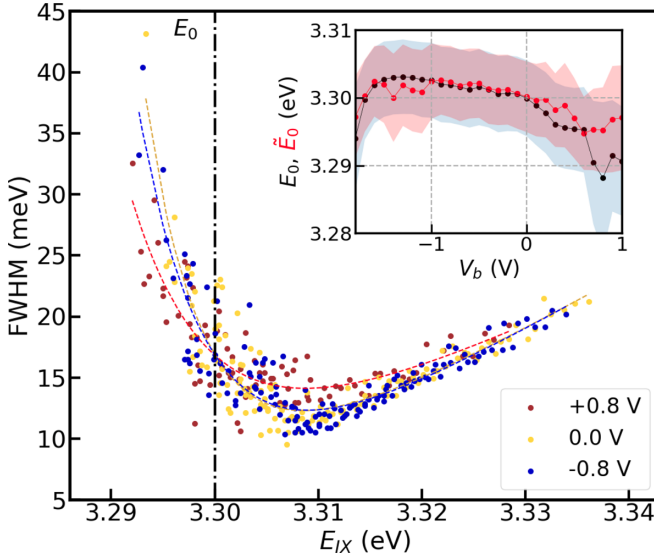


FIG. 13. Circles: IX linewidth as a function of its energy extracted from spatially-resolved PL shown in Figs. 6 and 7(b)–7(d). Dashed lines: fit to Eq. (A1). Vertical line shows the average zero-density value  $E_0$  used for the analysis of the trapping efficiency in Sec. III B. Inset: Parameter  $\tilde{E}_0$  (red) extracted from this fitting procedure and  $E_0$  extracted from  $I(E_{IX})$  analysis reported in the main text (black) as a function of the applied bias.

$D_s = M_x / (2\pi\hbar^2)$  is the two-dimensional density of states per spin,  $\hbar$  is the reduced Planck constant, and  $M_x$  is the in-plane mass of the exciton [31]. This yields  $\sigma_h \approx 45$ , almost an order of magnitude above the experimentally determined value. Similar results are reported in Ref. [31] for IXs hosted by GaAs-based heterostructures.

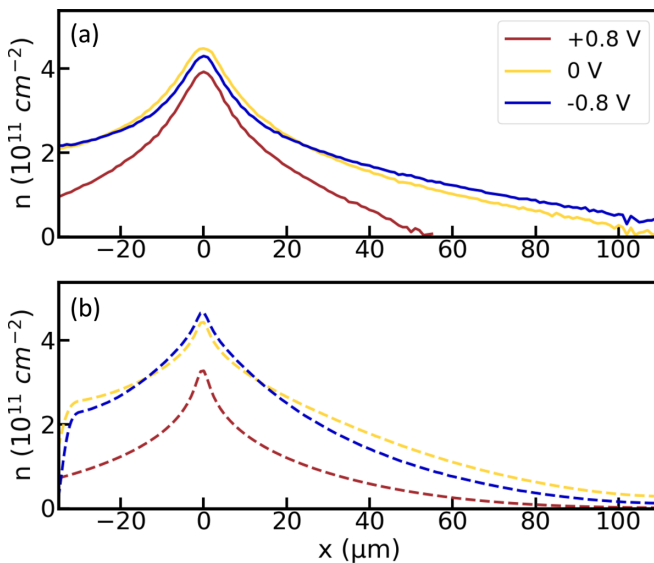


FIG. 14. Distribution of IX density within the trap  $n(x, y=0)$  measured (a) and calculated (b) for three different values of electric bias. Excitation spot is positioned at  $x=0$ . Experimental values of the IX density correspond to the data shown in Figs. 6(b)–6(d).

### 3. Drift-diffusion-losses modeling of the bias-controlled IX trapping

The bias-dependent IX trapping can be modeled within two-dimensional drift-diffusion-losses formalism. It is similar to the one used in our previous work, but includes two additional ingredients, namely bias-dependences of the in-plane potential and of the nonradiative recombination rate.

The equation for the IX density under optical pumping reads [10,67]:

$$\frac{\partial n}{\partial t} = -\nabla \cdot \mathbf{J} + G - Rn, \quad (\text{A5})$$

where  $R$  is the recombination rate,  $\mathbf{J}$  is the IX current density. The IX generation rate is  $G = (N_p / \pi a_0^2) \exp(-(x^2 + y^2)/a_0^2)$ , where  $N_p$  is the number of excitons generated per second and  $a_0 = 1 \mu\text{m}$  is the radius of the excitation spot centered at  $x = y = 0$ .

The exciton current  $\mathbf{J}$  contains drift and diffusion components:  $\mathbf{J} = \mathbf{J}_{\text{drift}} + \mathbf{J}_{\text{diff}}$ .

The IX diffusion current  $\mathbf{J}_{\text{diff}}$  characterized by the diffusion coefficient  $D$  is given by

$$\mathbf{J}_{\text{diff}} = -D\nabla n. \quad (\text{A6})$$

Here we use the value  $D = 0.4 \text{ cm}^2/\text{s}$  consistent with our previous work on the similar samples studied under similar conditions [39,44].

The drift term  $\mathbf{J}_{\text{drift}}$  in Eq. (A5) can be written as

$$\mathbf{J}_{\text{drift}} = -\mu n \nabla (\phi_0 n + U(x, y)), \quad (\text{A7})$$

where  $\mu = D/(k_B T)$  is the IX mobility and  $k_B$  is the Boltzmann constant. This current is due to both exciton-exciton interaction energy  $\phi_0 n$  and an external potential  $U(x, y) = U_{t0} U_{xy}$  imprinted by the electrodes. Here  $U_{t0}$  is the trap depth, and  $U_{xy}$  is normalized to unity.

The recombination rate  $R$  can be expressed in terms of radiative  $\tau_{\text{rad}}$  and nonradiative  $\tau_{\text{nr}}$  recombination times:

$$R = \frac{1}{\tau_r} + \frac{1}{\tau_{nr}}. \quad (\text{A8})$$

The density dependent radiative recombination time is given by  $\tau_r = \tau_{r0} \exp(-n/\gamma)$ , where  $\tau_{r0} = 1 \mu\text{s}$  is estimated from our previous work on similar samples [36] and  $\gamma$  is determined as described in the Appendix A1. The nonradiative recombination rate is assumed to depend exponentially on the absolute value of the in-plane component of the electric field  $F_{xy} = \nabla U(x, y)$ :

$$\frac{1}{\tau_{nr}} = \frac{1}{\tau_{nr0}} \exp\left(\frac{\|F_{xy}\|}{F_0}\right), \quad (\text{A9})$$

where  $\tau_{nr0}$  is the nonradiative recombination time in the absence of the in-plane electric field,  $F_0$  is a critical field leading to IX dissociation. The latter can be roughly estimated as a ratio between IX binding energy and in-plane Bohr radius, but *a priori* their values are unknown, and may be used as fitting parameters.

To solve numerically the drift-diffusion equation (A5), we proceed in two steps.

First, the in-plane potential  $U(x, y)$  and the corresponding in-plane electric field  $F_{xy}$  are calculated numerically by solving in three dimensions the Poisson equation. It turns out that

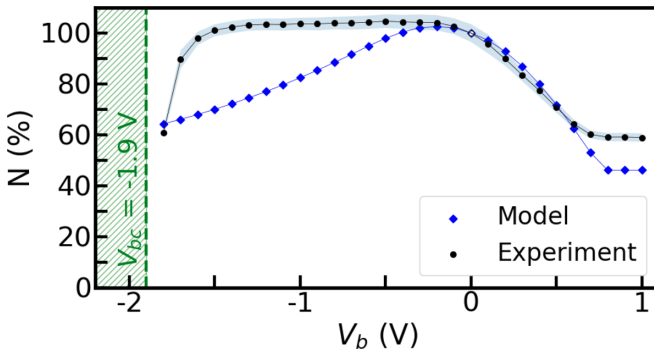


FIG. 15. IX population in the trap at  $y = 0$  integrated along the  $x$  axis (in percent of IX population at  $V_b = 0$ ), measured (black) and calculated (blue) as a function of applied bias. Experimental values are the same as in Fig. 9(a).

close to the trap edge  $U_{xy}$  is well approximated by the error function:

$$U_{xy} = \frac{1}{2} \left[ \operatorname{erf} \left( -\frac{r(x, y)}{\sqrt{2}\sigma} \right) + 1 \right], \quad (\text{A10})$$

where  $r(x, y)$  is the distance between the in-plane position  $(x, y)$  and the trap edge (using the relative normal coordinate) and  $\sigma \simeq 100$  nm is the standard deviation of the error function. The value of  $\sigma$  depends essentially on the distance between the QW and the top electrode. Note also that, for simplicity, this model neglects the density dependence of the trapping potential.

The second step consists of using a two-dimensional finite element method [68] to solve numerically Eq. (A5), in which

Eq. (A10) is injected considering  $\sigma$  as an additional parameter. The best agreement with experimental results is obtained by increasing  $\sigma$  up to  $2 \mu\text{m}$ . This reveals that the model overestimates the nonradiative recombination rate at high electric fields. We speculate, that accounting for the density dependence of  $\tau_{nr}$  could amend the agreement with the in-plane potential profile calculated from the Poisson equation. The values of over fitting parameters are  $N_p = 4 \times 10^{11} \text{ s}^{-1}$ ,  $\tau_{nr0} = 1 \mu\text{s}$  and  $F_0 = 30 \text{ kV/cm}$ .

The calculated steady-state solutions  $n(x, y)$  of the nonlinear Eq. (A5) are compared to the experimentally determined density profiles. Figure 14(a) shows IX density profiles  $n(x, y = 0)$  corresponding to the data shown in Figs. 6(b)–6(d), while Fig. 14(b) shows the results of the modeling. The comparison between measured and calculated integrated IX densities in the trap at different values of the applied electric bias is shown in Fig. 15.

The qualitative agreement between the model and the data can be ascertained. Namely, (i) strong reduction of IX population in the trap at  $V_b = +0.8$  V as compared to the absence of an external bias; (ii) a weak reduction of this population at  $V_b = -0.8$  V. The reduction of the trap depth from  $U_{t0} = 60$  meV at  $V_b = -0.8$  V to  $U_{t0} = 0$  meV at  $V_b = +0.8$  V is consistent with the experimental result  $R_e = 38$  meV/V, see Fig. 5.

However, a quantitative agreement could not be reached. In particular, the model yields much stronger reduction of the IX density at negative bias than observed experimentally. Elaboration of a more complex model taking account of density dependence of the in-plane electric field could be relevant for a better understanding of IX trapping and release.

- 
- [1] Y. J. Chen, E. S. Koteles, B. S. Elman, and C. A. Armiento, Effect of electric fields on excitons in a coupled double-quantum-well structure, *Phys. Rev. B* **36**, 4562 (1987).
- [2] A. Alexandrou, J. A. Kash, E. E. Mendez, M. Zachau, J. M. Hong, T. Fukuzawa, and Y. Hase, Electric-field effects on exciton lifetimes in symmetric coupled GaAs/Al<sub>0.3</sub>Ga<sub>0.7</sub>As double quantum wells, *Phys. Rev. B* **42**, 9225 (1990).
- [3] P. Rivera, J. R. Schaibley, A. M. Jones, J. S. Ross, S. Wu, G. Aivazian, P. Klement, K. Seyler, G. Clark, N. J. Ghimire, J. Yan, D. G. Mandrus, W. Yao, and X. Xu, Observation of long-lived interlayer excitons in monolayer MoSe<sub>2</sub>–WSe<sub>2</sub> heterostructures, *Nat. Commun.* **6**, 6242 (2015).
- [4] I. C. Gerber, E. Courtade, S. Shree, C. Robert, T. Taniguchi, K. Watanabe, A. Balocchi, P. Renucci, D. Lagarde, X. Marie, and B. Urbaszek, Interlayer excitons in bilayer MoS<sub>2</sub> with strong oscillator strength up to room temperature, *Phys. Rev. B* **99**, 035443 (2019).
- [5] D. Unuchek, A. Ciarrocchi, A. Avsar, K. Watanabe, T. Taniguchi, and A. Kis, Room-temperature electrical control of exciton flux in a van der Waals heterostructure, *Nature (London)* **560**, 340 (2018).
- [6] L. A. Jauregui, A. Y. Joe, K. Pistunova, D. S. Wild, A. A. High, Y. Zhou, G. Scuri, K. De Greve, A. Sushko, C.-H. Yu, T. Taniguchi, K. Watanabe, D. J. Needleman, M. D. Lukin, H. Park, and P. Kim, Electrical control of interlayer exciton dynamics in atomically thin heterostructures, *Science* **366**, 870 (2019).
- [7] A. A. High, A. T. Hammack, L. V. Butov, M. Hanson, and A. C. Gossard, Exciton optoelectronic transistor, *Opt. Lett.* **32**, 2466 (2007).
- [8] K. F. Mak and J. Shan, Opportunities and challenges of interlayer exciton control and manipulation, *Nat. Nanotechnol.* **13**, 974 (2018).
- [9] Z. Vörös, R. Balili, D. W. Snoke, L. Pfeiffer, and K. West, Long-Distance Diffusion of Excitons in Double Quantum Well Structures, *Phys. Rev. Lett.* **94**, 226401 (2005).
- [10] R. Rapaport, G. Chen, and S. H. Simon, Nonlinear dynamics of a dense two-dimensional dipolar exciton gas, *Phys. Rev. B* **73**, 033319 (2006).
- [11] C. J. Dorow, M. W. Hasling, D. J. Choksy, J. R. Leonard, L. V. Butov, K. V. West, and L. N. Pfeiffer, High-mobility indirect excitons in wide single quantum well, *Appl. Phys. Lett.* **113**, 212102 (2018).
- [12] K. Wagner, J. Zipfel, R. Rosati, E. Wietek, J. D. Ziegler, S. Brem, R. Perea-Causín, T. Taniguchi, K. Watanabe, M. M. Glazov, E. Malic, and A. Chernikov, Nonclassical Exciton Diffusion in Monolayer WSe<sub>2</sub>, *Phys. Rev. Lett.* **127**, 076801 (2021).

- [13] Z. Sun, A. Ciarrocchi, F. Tagarelli, J. F. Gonzalez Marin, K. Watanabe, T. Taniguchi, and A. Kis, Excitonic transport driven by repulsive dipolar interaction in a van der Waals heterostructure, *Nat. Photonics* **16**, 79 (2022).
- [14] A. A. High, J. R. Leonard, A. T. Hammack, M. M. Fogler, L. V. Butov, A. V. Kavokin, K. L. Campman, and A. C. Gossard, Spontaneous coherence in a cold exciton gas, *Nature (London)* **483**, 584 (2012).
- [15] R. Anankine, M. Beian, S. Dang, M. Alloing, E. Cambril, K. Merghem, C. G. Carbonell, A. Lemaître, and F. Dubin, Quantized Vortices and Four-Component Superfluidity of Semiconductor Excitons, *Phys. Rev. Lett.* **118**, 127402 (2017).
- [16] K. Cohen, Y. Shilo, K. West, L. Pfeiffer, and R. Rapaport, Dark hHigh density dipolar liquid of excitons, *Nano Lett.* **16**, 3726 (2016).
- [17] Y. Mazuz-Harpaz, K. Cohen, B. Laikhtman, R. Rapaport, K. West, and L. N. Pfeiffer, Radiative lifetimes of dipolar excitons in double quantum wells, *Phys. Rev. B* **95**, 155302 (2017).
- [18] Y. Shilo, K. Cohen, B. Laikhtman, K. West, L. Pfeiffer, and R. Rapaport, Particle correlations and evidence for dark state condensation in a cold dipolar exciton fluid, *Nat. Commun.* **4**, 2335 (2013).
- [19] M. Stern, V. Umansky, and I. Bar-Joseph, Exciton liquid in coupled quantum wells, *Science* **343**, 55 (2014).
- [20] S. Misra, M. Stern, A. Joshua, V. Umansky, and I. Bar-Joseph, Experimental Study of the Exciton Gas-Liquid Transition in Coupled Quantum Wells, *Phys. Rev. Lett.* **120**, 047402 (2018).
- [21] G. J. Schinner, J. Repp, E. Schubert, A. K. Rai, D. Reuter, A. D. Wieck, A. O. Govorov, A. W. Holleitner, and J. P. Kotthaus, Many-body correlations of electrostatically trapped dipolar excitons, *Phys. Rev. B* **87**, 205302 (2013).
- [22] L. V. Butov, Collective phenomena in cold indirect excitons, *J. Exp. Theor. Phys.* **122**, 434 (2016).
- [23] M. Combescot, R. Combescot, and F. Dubin, Bose-Einstein condensation and indirect excitons: a review, *Rep. Prog. Phys.* **80**, 066501 (2017).
- [24] Z. Wang, D. A. Rhodes, K. Watanabe, T. Taniguchi, J. C. Hone, J. Shan, and K. F. Mak, Evidence of high-temperature exciton condensation in two-dimensional atomic double layers, *Nature (London)* **574**, 76 (2019).
- [25] L. V. Butov, Excitonic devices, *Superlattices Microstruct.* **108**, 2 (2017).
- [26] Y. Liu, A. Elbanna, W. Gao, J. Pan, Z. Shen, and J. Teng, Interlayer excitons in transition metal dichalcogenide semiconductors for 2D optoelectronics, *Adv. Mater.* **34**, 2107138 (2022).
- [27] T. Huber, A. Zrenner, W. Wegscheider, and M. Bichler, Electrostatic exciton traps, *Physica Status Solidi (a)* **166**, R5 (1998).
- [28] A. T. Hammack, N. A. Gippius, S. Yang, G. O. Andreev, L. V. Butov, M. Hanson, and A. C. Gossard, Excitons in electrostatic traps, *J. Appl. Phys.* **99**, 066104 (2006).
- [29] A. A. High, E. E. Novitskaya, L. V. Butov, M. Hanson, and A. C. Gossard, Control of exciton fluxes in an excitonic integrated circuit., *Science* **321**, 229 (2008).
- [30] P. Andreakou, S. V. Poltavtsev, J. R. Leonard, E. V. Calman, M. Remeika, Y. Y. Kuznetsova, L. V. Butov, J. Wilkes, M. Hanson, and A. C. Gossard, Optically controlled excitonic transistor, *Appl. Phys. Lett.* **104**, 091101 (2014).
- [31] M. Remeika, J. R. Leonard, C. J. Dorow, M. M. Fogler, L. V. Butov, M. Hanson, and A. C. Gossard, Measurement of exciton correlations using electrostatic lattices, *Phys. Rev. B* **92**, 115311 (2015).
- [32] M. Leroux, N. Grandjean, M. Lügt, J. Massies, B. Gil, P. Lefebvre, and P. Bigenwald, Quantum confined Stark effect due to built-in internal polarization fields in (Al,Ga)N/GaN quantum wells, *Phys. Rev. B* **58**, R13371 (1998).
- [33] N. Grandjean, B. Damilano, S. Dalmaso, M. Leroux, M. Lügt, and J. Massies, Built-in electric-field effects in wurtzite Al-GaN/GaN quantum wells, *J. Appl. Phys.* **86**, 3714 (1999).
- [34] B. Gil, *III-Nitride Semiconductors and their Modern Devices* (Springer, Berlin, 2014).
- [35] F. Fedichkin, T. Guillet, P. Valvin, B. Jouault, C. Brimont, T. Bretagnon, L. Lahourcade, N. Grandjean, P. Lefebvre, and M. Vladimirova, Room-Temperature Transport of Indirect Excitons in (Al,Ga)N/GaN Quantum Wells, *Phys. Rev. Applied* **6**, 014011 (2016).
- [36] F. Fedichkin, P. Andreakou, B. Jouault, M. Vladimirova, T. Guillet, C. Brimont, P. Valvin, T. Bretagnon, A. Dussaigne, N. Grandjean, and P. Lefebvre, Transport of dipolar excitons in (Al,Ga)N/GaN quantum wells, *Phys. Rev. B* **91**, 205424 (2015).
- [37] A. Zrenner, P. Leeb, J. Schäfer, G. Böhm, and G. Weimann, Indirect excitons in coupled quantum well structures, *Surf. Sci.* **263**, 496 (1992).
- [38] E. V. Calman, C. J. Dorow, M. M. Fogler, L. V. Butov, S. Hu, A. Mishchenko, and A. K. Geim, Control of excitons in multi-layer van der Waals heterostructures, *Appl. Phys. Lett.* **108**, 101901 (2016).
- [39] F. Chiaruttini, T. Guillet, C. Brimont, B. Jouault, P. Lefebvre, J. Vives, S. Chenot, Y. Cordier, B. Damilano, and M. Vladimirova, Trapping dipolar exciton fluids in GaN/(AlGa)N nanostructures, *Nano Lett.* **19**, 4911 (2019).
- [40] A. Honold, L. Schultheis, J. Kuhl, and C. W. Tu, Collision broadening of two-dimensional excitons in a GaAs single quantum well, *Phys. Rev. B* **40**, 6442 (1989).
- [41] M. Koch, R. Hellmann, G. Bastian, J. Feldmann, E. O. Göbel, and P. Dawson, Enhanced energy and phase relaxation of excitons in the presence of bare electrons, *Phys. Rev. B* **51**, 13887 (1995).
- [42] R. Anankine, S. Dang, M. Beian, E. Cambril, C. G. Carbonell, A. Lemaître, and F. Dubin, Temporal coherence of spatially indirect excitons across Bose-Einstein condensation: the role of free carriers, *New J. Phys.* **20**, 073049 (2018).
- [43] S. Birner, T. Zibold, T. Andlauer, T. Kubis, M. Sabathil, A. Trellakis, and P. Vogl, nextnano: General purpose 3-d simulations, *IEEE Trans. Electron Devices* **54**, 2137 (2007).
- [44] F. Chiaruttini, T. Guillet, C. Brimont, D. Scalbert, S. Cronenberger, B. Jouault, P. Lefebvre, B. Damilano, and M. Vladimirova, Complexity of the dipolar exciton Mott transition in GaN/(AlGa)N nanostructures, *Phys. Rev. B* **103**, 045308 (2021).
- [45] A. C. Schmitz, A. T. Ping, M. A. Khan, Q. Chen, J. W. Yang, and I. Adesida, Schottky barrier properties of various metals on n-type GaN, *Semicond. Sci. Technol.* **11**, 1464 (1996).
- [46] N. Miura, T. Nanjo, M. Suita, T. Oishi, Y. Abe, T. Ozeki, H. Ishikawa, T. Egawa, and T. Jimbo, Thermal annealing effects on Ni/Au based Schottky contacts on n-GaN and AlGaIn/GaN with insertion of high work function metal, *Solid-State Electron.* **48**, 689 (2004).
- [47] K. A. Rickert, A. B. Ellis, J. K. Kim, J.-L. Lee, F. J. Himpsel, F. Dwikusuma, and T. F. Kuech, X-ray photoemission

- determination of the Schottky barrier height of metal contacts to n-GaN and p-GaN, *J. Appl. Phys.* **92**, 6671 (2002).
- [48] F. Medjdoub, M. Zegaoui, B. Grimbert, N. Rolland, and P.-A. Rolland, Effects of AlGaN Back Barrier on AlN/GaN-on-silicon high-electron-mobility transistors, *Appl. Phys. Express* **4**, 124101 (2011).
- [49] P. Lefebvre, S. Kalliakos, T. Bretagnon, P. Valvin, T. Taliercio, B. Gil, N. Grandjean, and J. Massies, Observation and modeling of the time-dependent descreening of internal electric field in a wurtzite GaN/Al<sub>0.15</sub>Ga<sub>0.85</sub>N quantum well after high photoexcitation, *Phys. Rev. B* **69**, 035307 (2004).
- [50] W. Liu, R. Butté, A. Dussaigne, N. Grandjean, B. Deveaud, and G. Jacopin, Carrier-density-dependent recombination dynamics of excitons and electron-hole plasma in m-plane InGaN/GaN quantum wells, *Phys. Rev. B* **94**, 195411 (2016).
- [51] L. V. Butov, A. A. Shashkin, V. T. Dolgoplov, K. L. Campman, and A. C. Gossard, Magneto-optics of the spatially separated electron and hole layers in GaAs/Al<sub>x</sub>Ga<sub>1-x</sub>As coupled quantum wells, *Phys. Rev. B* **60**, 8753 (1999).
- [52] See Supplemental Material at <http://link.aps.org/supplemental/10.1103/PhysRevB.106.035429> for the corresponding animation, including 40 spatially resolved PL spectra (color encoded in log scale) measured upon excitation through the semitransparent electrode at applied electric bias varying from  $V_b = -3$  V to  $V_b = 0.9$  V at the excitation power  $P = 3.8$  mW.
- [53] More sophisticated full numerical calculation using Nextnano++ software [43] yields much smaller variation rate  $\mathcal{R}_e = ed/\mathcal{L} = 14$  meV/V, see Fig. 1(c).
- [54] IX densities reached in these experiments remain below exciton Mott transition, consequently we neglect eventual density-dependence of the IX binding energy.
- [55] This behavior could result from some spurious spread of the electric field from the metal-covered area towards bare surface regions.
- [56] C. Weisbuch, S. Nakamura, Y.-R. Wu, and J. S. Speck, Disorder effects in nitride semiconductors: Impact on fundamental and device properties, *Nanophotonics* **10**, 3 (2021).
- [57] See Supplemental Material at <http://link.aps.org/supplemental/10.1103/PhysRevB.106.035429> for the corresponding animations, including 40 spatially resolved PL spectra (color encoded in log scale) measured upon excitation within the trap at applied electric bias varying from  $V_b = -3$  V to  $V_b = 0.9$  V at two different excitation powers,  $P = 2.4$  mW and  $P = 0.6$  mW.
- [58] M. Remeika, J. C. Graves, A. T. Hammack, A. D. Meyertholen, M. M. Fogler, L. V. Butov, M. Hanson, and A. C. Gossard, Localization-Delocalization Transition of Indirect Excitons in Lateral Electrostatic Lattices, *Phys. Rev. Lett.* **102**, 186803 (2009).
- [59] B. Laikhtman and R. Rapaport, Exciton correlations in coupled quantum wells and their luminescence blue shift, *Phys. Rev. B* **80**, 195313 (2009).
- [60] A. L. Ivanov, E. A. Muljarov, L. Mouchliadis, and R. Zimmermann, Comment on “Photoluminescence Ring Formation in Coupled Quantum Wells: Excitonic Versus Ambipolar Diffusion”, *Phys. Rev. Lett.* **104**, 179701 (2010).
- [61] M. Beian, M. Alloing, R. Anankine, E. Cambril, C. G. Carbonell, A. Lemaître, and F. Dubin, Spectroscopic signatures for the dark Bose-Einstein condensation of spatially indirect excitons, *EPL* **119**, 37004 (2017).
- [62] A. A. High, A. T. Hammack, L. V. Butov, L. Mouchliadis, A. L. Ivanov, M. Hanson, and A. C. Gossard, Indirect excitons in elevated traps, *Nano Lett.* **9**, 2094 (2009).
- [63] A. L. Ivanov, Thermalization and photoluminescence dynamics of indirect excitons at low bath temperatures, *J. Phys.: Condens. Matter* **16**, S3629 (2004).
- [64] V. Savona, Effect of interface disorder on quantum well excitons and microcavity polaritons, *J. Phys.: Condens. Matter* **19**, 295208 (2007).
- [65] Z. Vörös, D. W. Snoke, L. Pfeiffer, and K. West, Direct Measurement of Exciton-Exciton Interaction Energy, *Phys. Rev. Lett.* **103**, 016403 (2009).
- [66] B. F. Gribakin, E. S. Khrantsov, A. V. Trifonov, and I. V. Ignatiev, Exciton-exciton and exciton-charge carrier interaction and exciton collisional broadening in GaAs/AlGaAs quantum wells, *Phys. Rev. B* **104**, 205302 (2021).
- [67] A. L. Ivanov, Quantum diffusion of dipole-oriented indirect excitons in coupled quantum wells, *Europhys. Lett.* **59**, 586 (2002).
- [68] F. Hecht, New development in freefem++, *J. Numer. Math.* **20**, 251 (2012).